Journal of Magnetism and Magnetic Materials 471 (2019) 444–449

Contents lists available at ScienceDirect

Journal of Magnetism and Magnetic Materials

journal homepage: www.elsevier.com/locate/jmmm

Research articles

Evaluation of a separate-receive coil by magnetic particle imaging of a solid phantom

Olaf Kosch[a,*], Hendrik Paysen[a], James Wells[a], Felix Ptach[a], Jochen Franke[b], Lucas Wöckel[c], Silvio Dutz[c], Frank Wiekhorst[a]

[a] Physikalisch-Technische Bundesanstalt, Berlin, Germany
[b] Bruker BioSpin, Ettlingen, Germany
[c] Institute of Biomedical Engineering and Informatics, Technische Universität Ilmenau, Germany

ARTICLE INFO

Keywords:
Magnetic Particle Imaging (MPI)
Image resolution analysis
Long-term stable phantom
Separate receive coil
Magnetic nanoparticles

ABSTRACT

To aid the optimization and development of Magnetic particle imaging (MPI), an accurate and translatable apparatus and a methodology for the characterisation of imaging quality are required. This requires magnetic nanoparticles (MNP) as imaging tracer for MPI measurements in a long-term stable, defined state, since MNP in liquid suspension might tend to change their magnetic properties over time, e.g. as a result of particle aggregation, sedimentation, or disintegration. To this end, we have developed solid phantoms containing freeze-dried perimag in mannitol for the comparison of resolution capabilities between different MPI scanners. Freeze drying of MNP was determined to be the optimal immobilisation method for maintaining the dynamic magnetic properties of MNP as compared with polymer or starch techniques.

Freeze-drying preserves the particle distribution, preventing the particles from aggregation or precipitation. Two different types of phantoms were developed, one (cross shaped) to seek for artefacts within reconstructed images, and one (coil shaped) to test the resolution limit. The resolution limit is determined from the coil phantom by measuring the smallest resolvable gap between the two adjacent tracer regions. Our resolution phantom contained a 2 mm wide channel filled with tracer. By using this phantom, the imaging performance of the preclinical MPI system and a prototype gradiometric separate receive coil installed within the same MPI scanner was determined. We found 2.1–2.2 mm resolution limit using the conventional set-up and 0.5–0.6 mm for the separate receive coil resulting in an improvement by factor four. Additionally, the resolution dependency on the channel wide was tested by a second resolution phantom contained a 1 mm wide channel. The long-term stability of the phantoms will be continuously monitored and improved.

1. Introduction

Magnetic particle imaging (MPI) is an emerging tomographic imaging technique capable of quantitatively determining the 3D distribution of a magnetic nanoparticle (MNP) based tracer material. MPI technology is still under development, and requires significant improvements, especially of the signal to noise ratio (SNR). To analyse the benefit of such improvements, we have completed our MPI benchmark system by a resolution analysis.

The preclinical MPI system (Bruker MPI 25/20 FF) installed at Charité University Hospital Berlin has recently been extended by the addition of a prototype gradiometric coil system as a separate signal-receive unit [1,2]. This differs from the established scanner design, in which excitation field generation and signal collection are both conducted by a single coil (TxRx-coil). As previously shown [2], the new receive unit uses a dedicated separate receive coil (Rx-coil) with a gradiometric design to decouple the excitation field. The Rx-coil was shown to increase the sensitivity of the system by +12 dB; and detection limit of image reconstruction based on iron quantity in the sample was improved from 133 ng for the TxRx-coil to 20 ng for the Rx-coil.

While significant advances have been made in MPI hardware development and image reconstruction, an unmet need remains for a toolset to quantitatively characterise the imaging performance offered by individual MPI scanners and imaging protocols, and to facilitate interlaboratory comparisons of MPI scanners. A number of obstacles must be overcome to achieve this. MNPs in liquid suspension are unstable over time [3], especially when subjected to magnetic excitation fields such as those found in MPI scanners. Aggregation, sedimentation

* Corresponding author.
E-mail address: olaf.kosch@ptb.de (O. Kosch).

https://doi.org/10.1016/j.jmmm.2018.09.114
Received 22 June 2018; Received in revised form 6 September 2018; Accepted 28 September 2018
Available online 29 September 2018

and other temporal changes in the particle structure or composition can dramatically alter their MPI performance. This hinders the comparison of imaging protocols, testing of scanner stability and the circulation of reference samples for cross-comparison between different scanners. Highly stable and well characterized reference materials and imaging phantoms are a necessity for MPI development to progress, and the technology to realise its full clinical potential.

To counter this need, we developed an imaging phantom which is designed for use in the analysis of MPI scanner resolution. With the goal of achieving long-term temporal stability, the immobilisation of MNPs was used to prevent particle migration or sedimentation, and to remove the risk of suspension fluid evaporation from the phantom. However, immobilisation of MNPs commonly produces dramatic losses in the quality of the MPI signals produced, which is counterproductive to the evaluation of scanners or imaging protocols. The aim of this work was to avoid these huge losses in the MPI signal, and to establish a particle system and immobilisation method which still offered good quality imaging signals.

A resolution phantom is necessary combining long-term stability and ability of hi-resolution to get the benefit in image quality of an improved MPI instrumentation, like by a separate receive coil. Further is a long-term stable phantom employable for comparison of different MPI scanners.

Note, the achievable resolution is heavily dependent on the MNP type, immobilisation state and concentration used to fill the phantom, the width and depth of the phantom channel, and the MPI imaging parameters used.

2. Materials and methods

2.1. Phantoms and MPS measurements

The MNP type perimag (micromod, Rostock, Germany) was used in all of the reported studies. Three different immobilisation methods were tested on the perimag MNPs: 1. by synthetic polymer elastosil RT604 (Wacker Chemie AG, München, Germany) [4], 2. By modified starch blends [5] and 3. freeze-dried in a sugar matrix of mannitol. The iron content of each immobilized samples was elasosil c (Fe) = 200 mmol/L, starch c(Fe) = 40 mmol/L for the starch sample and freeze-dried c(Fe) = 76.1 mmol/L. The different iron content is related to the process steps of the different immobilization procedures and the aim to achieve a strong MPI/MPS signal. A sample of perimag MNPs in their original liquid suspension c(Fe) = 152.2 mmol/L was also measured for comparison. We analysed the dynamic magnetisation behaviour of the immobilised MNP by magnetic particle spectroscopy (MPS) [6] to get a raw characterisation of the imaging properties [7]. We used a commercial MPS device (MPS-3, Bruker BioSpin) operating at a fixed excitation frequency of f_0 = 25.25 kHz (identical to the drive field frequency in z- direction of our MPI and related to the sampling frequency 2.5 MHz divided by 99) and variable excitation field amplitudes B_{ex} between 0.05 mT and 25 mT [8]. In the reported measurements an MPS excitation field of B_{ex} = 12 mT was used as it is a common excitation amplitude in commercial MPI scanners. MPS measurements used 30 µL samples filled into PCR cups, with data averaging of 10 s.

Three phantom geometries were designed, and produced via 3D printing. Channels in each phantom were filled with freeze-dried perimag in mannitol with c(Fe) = 76.1 mmol/L. Two of the phantoms implemented a channel with a width and depth of 2 mm, and the third phantom had a channel depth and width of 1 mm. The first phantom used four channels in the shape of a cross (Fig. 1a)) and is filled with four times 45 µL freeze-dried perimag. The minimum distance between the corners is 2 mm. The first phantom was printed on a 3D printer (Raise3D N2 Plus, Raise3D INC., Costa Mesa, USA) using filaments of polylactide (filamentworld, Neu-Ulm, Germany). The geometry with the corners and straight lines was chosen to enable a fast detection of imaging artefacts.

The second phantom (Fig. 1b) was designed to achieve a resolution limit defined by the minimal detectable gap in the structure. It was printed using white photoactive resin using a Form 2 Desktop SLA 3D-printer (FormLabs, Somerville, USA). After 3D printing the whole parts were post-cured with irradiation from an incubator (Otoflash G171, EnvisionTEC, Detroit, USA) to improve stability, because the cross-linking of the polymers is assisted by UV-light treatment.

The phantom has a channel cross-section of 2 × 2 mm^2, it contains freeze dried perimag. The design consists of a channel forming an exponential growing spiral, where the gap varies from 0.36 to 6.0 mm. Using this layout, the read out of the gap distance is supported by position and additionally by angle in the spiral. An illustration of the second phantom design is shown in Fig. 2a).

The third phantom consists of a channel with a cross-section of 1 × 1 mm^2 in an exponential growing spiral. The phantom was printed using clear photoactive resin in the same Form 2 Desktop SLA 3D-printer (FormLabs, Somerville, USA) as phantom 2, the additional light source for added stability was again used. The spiral of the phantom was filled with freeze-dried perimag. The aim of the phantom was to demonstrate the differences in resolution obtained when imaging thinner structures. A diagram of phantom 3 is shown in Fig. 2b).

2.2. Magnetic particle imaging

2.2.1. MPI measurements

All MPI measurements were performed using a preclinical MPI system (Bruker MPI 25/20 FF) installed at Charité University Hospital Berlin. This system is based on the movement of a field-free-point (FFP) through the whole imaging volume, and employs the system function (SF) approach for image reconstruction [9,10]. A selection gradient field of 2.5 T/m/μ_0 in the z-direction and 1.25 T/m/μ_0 in x- and y-directions, (see coordinate system Fig. 3a)) is used to generate the FFP, and was implemented for all measurements presented in this work. By moving the FFP through the field of view (FOV), a spatially encoded signal of the whole imaging volume can be detected. This movement of the FFP on a closed 3D Lissajous-trajectory is accomplished by applying three orthogonal drive-fields oscillating at slightly different excitation frequencies (2.5 MHz divided by 102/96/99 in x-/y-/z-direction) with amplitudes of 12 mT/μ_0. Thus, in case of a 3D acquisition scheme one total Lissajous-trajectory is completed after a period of 21.5 ms, allowing the reconstruction of a full 3D dataset of the FOV. The separate Rx-coil (Fig. 3b)) has a gradiometer design consisting of an inner pick-up coil (Ø = 72 mm, 2 × 13 turns of copper litz-wire reducing the eddy currents at high frequency) connected in series with an outer cancelation coil (Ø = 104 mm, 2 × 6 turns of copper litz-wire with reverse winding direction) [2]. This cancelation coil eliminates almost the induced signal by the excitation field. The application of this separate gradient coil prevents the galvanic coupling between transmit- and receive circuit and thus reduces the noise level.

However, the main factor of the improved sensitivity results from the smaller diameter of the pick-up coil, because more of the magnetic flux of the MNPs is detected inside a smaller coil surface without the return of the flux lines inside the coil surface (s. Fig. 4). Only flux lines which return outside of the coil contribute to the measured signal. Flux loops which return inside of the coil do not contribute to the measured signal. Using a smaller coil increased the number of field lines which return outside of the coil, and thus increases the size of the measured signal. Conversely, smaller coils will also reduce the size of the sensitive region of the pick-up unit, with a subsequent impact on the imaging quality. These two considerations should be balanced in order to achieve the optimal Rx coil diameter for a given application. Related to the coil diameter of the original TxRx-coil (Ø = 160 mm), the coil surface of the Rx-coil is by more than factor 4 smaller. It was already shown before in [11] to achieve an even higher sensitivity by a smaller diameter (Ø = 40 mm). However, this leads to a smaller accessible

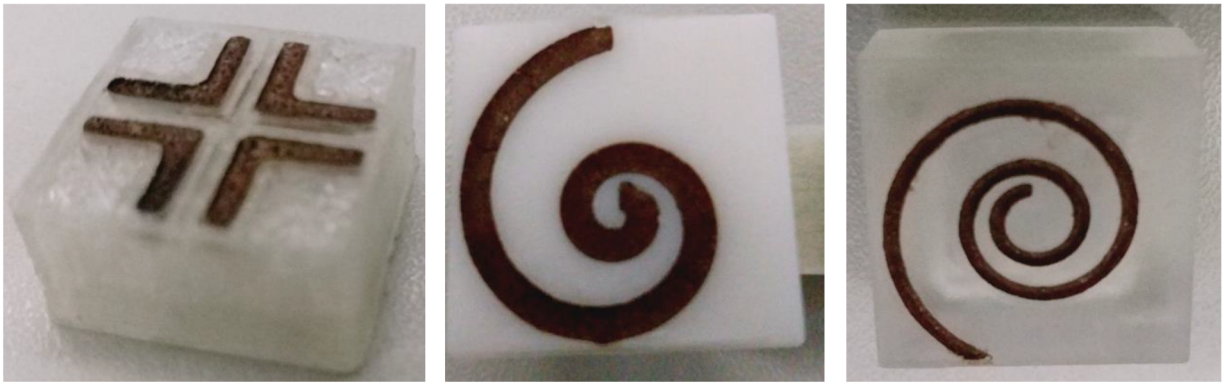

Fig. 1. a) Filled cross- phantom 2 mm channel, b) resolution phantom with exponential growing spiral layout and 2 mm channel width and c) 1 mm channel phantom with exponential growing spiral.

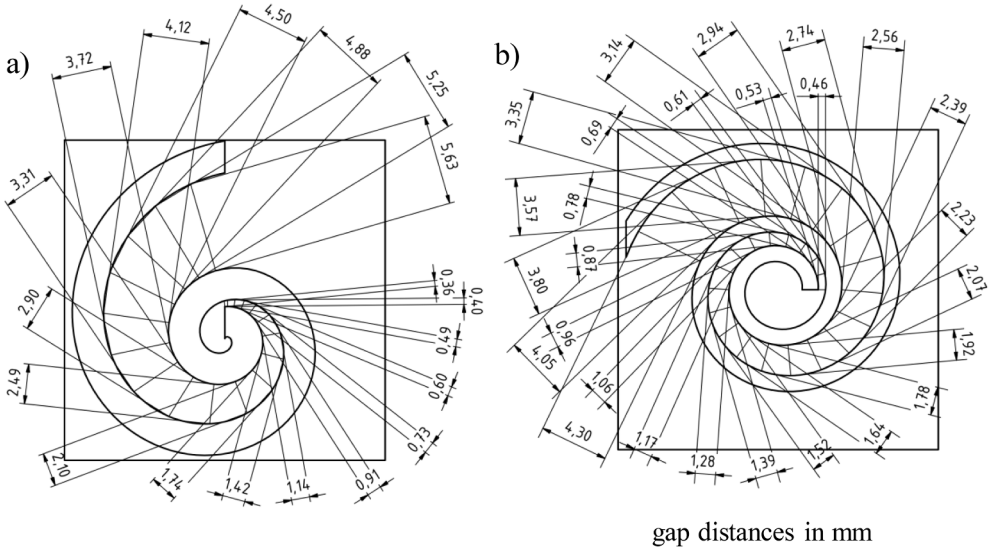

Fig. 2. Diagrams of gap distances a) of phantom 2 with 2 × 2 mm^2 channel cross-section and b) phantom 3 with 1 × 1 mm^2 channel cross-section.

bore. In our case the Rx-coil is positioned along the *x*-axis of the scanner, the accessible bore is reduced to Ø = 65 mm (compared to 120 mm without Rx-coil).

A SF was measured for use in all image reconstructions of the phantoms. This SF was measured using a reference sample of 13.5 µL freeze-dried perimag in mannitol, (c(Fe) = 76.1 mmol/L) within a 3 × 3 × 1.5 mm^3 container. The reference sample was robotically positioned at 33 × 33 × 33 individual positions in a FOV of 26.4 × 26.4 × 13.2 mm^3 resulting in a voxel size of 0.8 × 0.8 × 0.4 mm^3. This includes an overscan [12] of the physical FOV of 19.2 × 19.2 × 9.6 mm^3 using the chosen gradient field and drive field. For each position, 100 measurement repetitions were acquired and averaged. The data acquisition at each point was performed using the TxRx-coil and separate Rx-coil (Fig. 3b)) simultaneously. Background measurements of the empty scanner were acquired intermittently throughout the SF acquisition after every 33th measured position. These were used to subtract (long-lasting) background contributions from the signals, and to calculate the signal-to-noise ratio

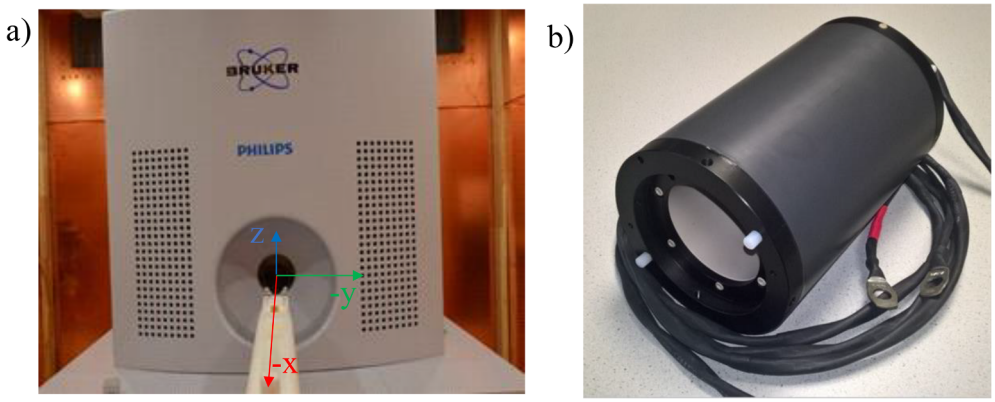

Fig. 3. a) MPI-scanner Bruker MPI 20/25 FF and coordinate system (*x*- and *y*- direction inverted shown) and b) the prototype of the separate receive coil.

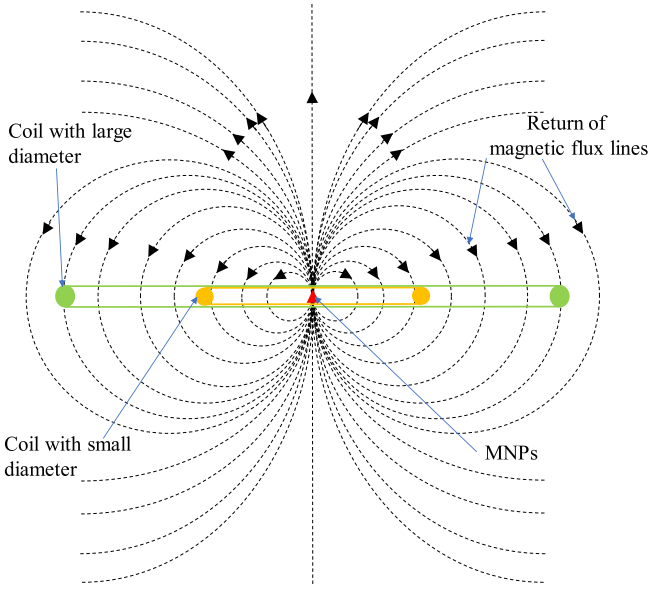

Fig. 4. Dependency of captured magnetic flux lines of the MNPs related to the coil diameter.

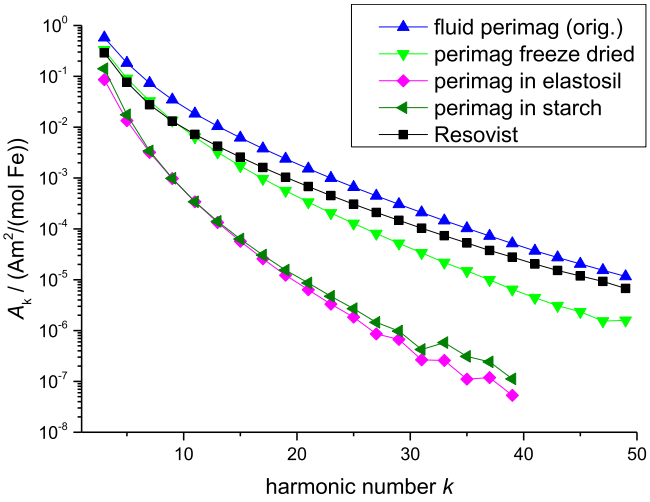

Fig. 5. Spectra of perimag in different states measured by MPS at 12 mT, together with the commonly used MPI tracer Resovist in liquid dispersion (c (Fe) = 10 mmol/L). For better comparison the spectra have been normalised to the iron concentration of the individual samples.

(SNR) for all frequency components. The measurement time of the SF was more than 38 h.

The measurements of the phantoms were performed using the same field parameter as the SF, and again data acquisition was performed using the TxRx-coil and Rx-coil simultaneously. At the beginning of each measurement, we recorded the background signal and then the phantom was moved robotically to the centre of the FOV. The background was removed from the recorded data in a processing step during the reconstruction.

2.3. Image reconstruction

Image reconstructions were performed using the Kaczmarz-algorithm with Tikhonov regularisation in the ParaVision 6 MPI software (Bruker). The data of each coil type were used separately for reconstructions, to provide a comparison of the imaging capabilities of each. The frequency components used in the reconstruction process were selected by a minimum SNR threshold based on the SNR calculated for all frequency components in the SF. The SNR threshold was chosen due to the biggest distortions in the measured spectra induced by the excitation fields, all components below 70 kHz were neglected. All reconstructions were calculated with 20 Kaczmarz iterations to force high resolution imaging by a high number of iterations. A fixed SNR threshold of four and the regularisation factor of 10^{-5} were chosen for the reconstruction of the first and the second phantom to enclose as many frequency components as possible for a benefit of a detailed reconstruction result. By this SNR threshold 1847 frequency components were selected using only the data of the original TxRx-coil and 4022 frequency components using only the data of the separate Rx-coil in the reconstructions due to the higher sensitivity of the separate Rx-coil. The very small regularisation factor was applied to avoid broader resulting distributions due to the regularisation limiting the capability to resolve smaller structures. For the third phantom it was necessary to increase the regularisation factor to 10^{-4} and the SNR threshold to 5 due to the lower amount of MNPs in the channel cross-section resulting in smaller signals. Note, the selection of the frequency components by the threshold is based on the SNR of the SF. If the signal and the SNR in the MPI measurement of the phantom is changed, we have to adapt the SNR threshold.

3. Results and discussions

3.1. MPS

The characterisation of the MNPs in the different immobilisation media by MPS give an estimation of the MPI performance. The measured spectra normalised to the iron concentration for each perimag preparation, and the spectrum of Resovist (Meito Sangyo, Japan, c (Fe) = 10 mmol/L) as the gold standard in MPI are shown in Fig. 5.

If the normalised spectra of the immobilized MNPs are similar to Resovist or even better (higher third harmonic amplitude, and lower decay of higher harmonics) we can expect a high resolution enabled imaging. The fluid perimag spectrum is about twice the spectrum of Resovist. The spectrum of freeze-dried perimag in mannitol is very similar to Resovist, only in the higher harmonics a relative successive growing decay is visible. In this regard, only harmonics up to approximately the 20th–25th order (depending on the MNP type) provide a benefit for MPI reconstruction due to the reduced SNR of MPI related to MPS, even for our MPI system containing the separate receive coil. Without the separate Rx-coil only harmonics up to the 16th–21st order of the spectra contribute beneficial to the image reconstruction (See Fig. 5).

For all immobilised samples, the spectral amplitudes are lower than for the fluid sample. This is because the Brownian rotation of the MNP is blocked due to the immobilisation, which limits the dynamic response of the MNPs to an external oscillating magnetic field.

The spectra of perimag embedded in elastosil or starch depict significant lower amplitudes, and a very pronounced decay of the higher harmonics, as compared with the particles immobilised by freeze drying. The exact mechanism for this is currently unclear, but agglomeration of the particles during preparation of elastosil and starch samples is a likely cause.

Freeze-dried perimag was therefore selected for use in the MPI phantoms, because the spectrum has only moderate losses in the amplitudes compared to original perimag dispersed in water. The expected MPI performance should therefore be close to the performance of Resovist. The sugar-matrix of freeze-dried MNPs in mannitol is sensitive to water. By this reason a dry storage is mandatory for the phantoms. Immobilised MNPs in elastosil and starch are more resistant to water and mechanical stress.

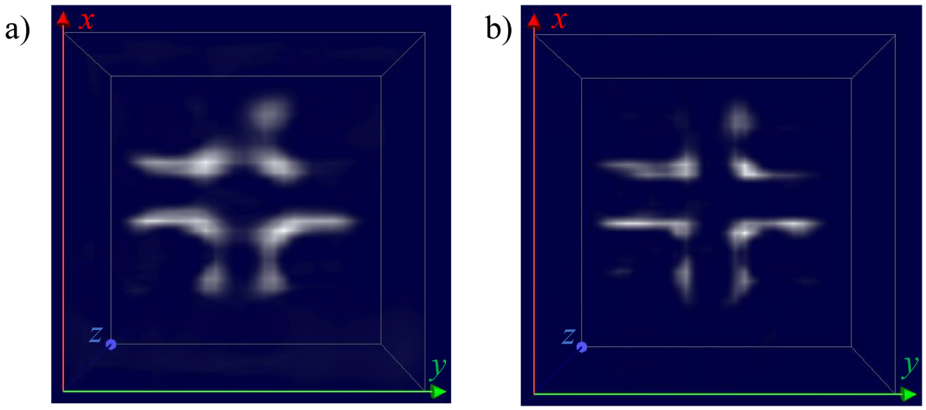

Fig. 6. Reconstructed images of the phantom 1 (cross) filled with freeze-dried perimag based on data of a) original TxRx-coil and b) separate Rx-coil.

3.2. MPI

The phantoms were placed in the centre of the FOV, in the *xy*- plane. The reconstructed image of the first phantom is shown as intensity plot in Fig. 6 with viewing in *z*- direction. Fig. 6 a) depicts the result using the data of the original TxRx- coil and b) the result for the separate Rx-coil.

For the TxRx data, the four parts of the object are not clearly separated within the reconstructed image. This is particularly visible along the *y*- axis. In addition, many of the straight lines of the phantom appear distorted.

Of course, a higher resolution can be achieved in *z*-direction, e.g. by placing the phantom in the *xz*-plane because the gradient field in *z*-direction is doubled than in *x*- and *y*- direction. However, the size of the FOV in *z*- direction is only the half related to *x* and *y*. Reconstructing the data from the simultaneous Rx-coil measurement, we achieve significant improvements in the reconstruction, with straight edges and four separate sharp corners. The intensity differences in the four corners are likely to be the result of an uneven distribution of the MNPs in the channels.

Phantom 2 was used to study the resolution capability. For this purpose, reconstructions using either the TxRx-coil or the Rx-coil data were formatted to show the volume where the intensity value is not lower than 20% of the maximum intensity (Bruker, ParaVision Software, using the isolevel-feature), (Fig. 7a) and b)). Note, for the ideal reconstruction result the value in the gap between the channels should be 0%. However, this is out of reach due to noise in the real measurement data. The isolevel threshold of 20% was selected in order to keep the regularisation factor as small as possible. A higher regularisation factor reduces the noise in the image, however it makes the reconstructed distribution broader, and thus reduces the achievable resolution. The limit of resolution can be estimated from the distance at which the two channels fuse to one and the inner channel stops as the gap between them is no longer visible in the reconstructed image. The real separation of the channels at that location in the phantom can then be read off from the diagram of gap distances in Fig. 2. Note, by varying the isolevel value the fusion of the channels is less or more visible, however the position where the inner channel stops will not change.

This method yields a resolution limit (in terms of object separation) for the 2 mm phantom of about 2.1–2.3 mm using the TxRx-coil data, and 0.5–0.6 mm for the Rx-coil data. This suggests that the Rx coils offers a significant advantage in resolving objects, particularly when located close together. The determined resolution values include an interpolation because the size of the voxel in the SF is 0.8 mm in *x*- and *y*- direction. However, we could not observe significant changes by a shift of the phantom in the FOV.

The reconstructed volumes of phantom 3 with a channel cross-section of $1 \times 1\,\mathrm{mm}^2$ are shown in Fig. 8. The amount of MNP in the $1 \times 1\,\mathrm{mm}^2$ channel cross-section is reduced by factor of 4 compared with phantom 2.

Noise becomes visible in the imaging result of this phantom, due to the smaller amount of tracer in the channel cross-section; and the smaller resulting signals. Here, it was necessary to increase the regularisation factor to 10^{-4}. By utilising a higher regularisation factor, the resolution will be worse. The resolution is nonetheless influenced by the noise. We achieve for phantom 3 a resolution limit of 2.7–2.8 mm applying the data of the TxRx-coil and 1.1–1.2 mm for the Rx-coil (see Fig. 2b).

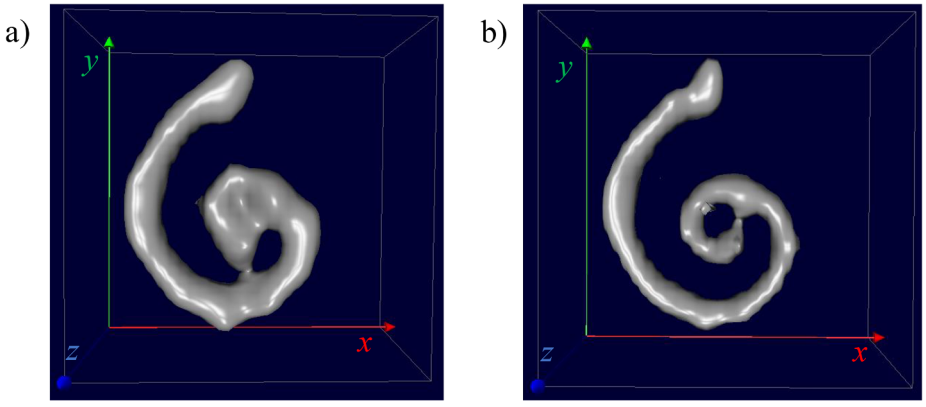

Fig. 7. Reconstructed volume of phantom 2 using the data of a) the TxRx-coil and b) the Rx-coil.

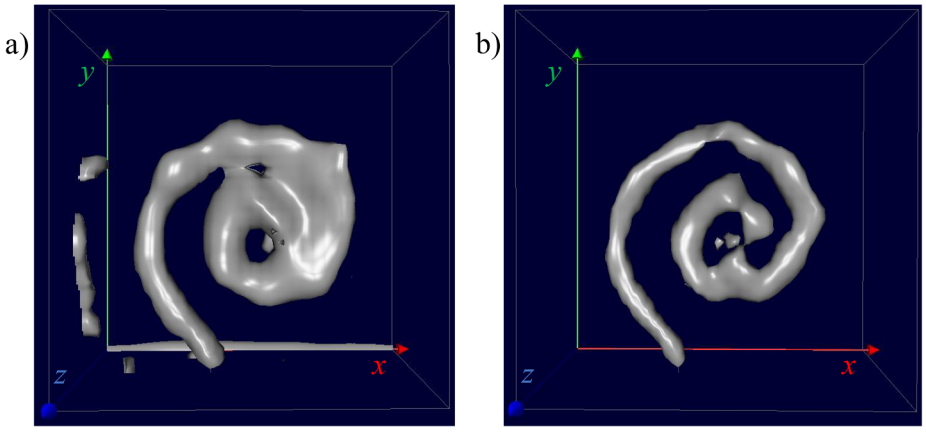

Fig. 8. Reconstructed volume of phantom 3 with $1 \times 1\,mm^2$ channel cross-section using the data of a) the TxRx-coil and b) the Rx- coil.

4. Conclusions

By employing freeze-dried perimag in a structure using a channel cross-section of $2 \times 2\,mm^2$, a resolution phantom is established with reliable MPI reconstruction. Utilising this phantom, we have developed a procedure to estimate the resolution limit of the MPI hardware enabling multi-site comparison. By the prototype of the separate Rx-coil, we achieve a resolution increase by the factor of about four compared to the original TxRx-coil of the preclinical MPI system (Bruker MPI 25/20 FF).

Note, there is a dependency of the resolution on the amount of tracer (concentration and cross-section of the tracer channel). When reducing the structure width to 1 mm, the image reconstructions become less reliable due to the domination by noise. Alternately, the 1 mm phantom could be successfully imaged by applying MNPs at a higher concentration. Thus, the resolution depends on the amount of MNPs. The best resolution requires a high amount of MNPs.

The future work is the SF measurement with smaller voxel size in *x*- and *y*- direction to make the estimation of resolution for very small gap distances more reliable. Further, we plan to improve the processing steps for perimag in elastosil or rather starch to achieve a high chemical and mechanical resistance and to keep the magneto-dynamic behaviour similar to freeze-dried perimag. The long-term stability of the freeze-dried material is currently under evaluation.

Acknowledgements

Funding: This research was supported by German Research Foundation (DFG) grants “quantMPI: Establishment of quantitative Magnetic Particle Imaging (MPI) application oriented phantoms for preclinical investigations”, TR 408/9-1 and DU1293/6-1 and “AMPI: Magnetic particle imaging: Development and evaluation of novel methodology for the assessment of the aorta in vivo in a small animal model of aortic aneurysms “, SHA 1506/2-1 and by DFG priority program “SPP 1681: Field Controlled Particle Matrix Interaction: Synthesis, Multi-Scale Modelling and Application of Magnetic Hybrid-Materials ”, WI 4230/1-3 and the EMPIR program MagNaStand: Towards an ISO standard for magnetic nanoparticles (grand no. 16NRM044).

References

[1] J. Wells, H. Paysen, O. Kosch, N. Löwa, F. Schmitzberger, M. Makowksi, J. Franke, L. Trahms, F. Wiekhorst, Characterizing a preclinical magnetic particle imaging system with separate pickup coil, IEEE Trans. Magn. 53 (2017), https://doi.org/10.1109/TMAG.2017.2708419.

[2] H. Paysen, J. Wells, O. Kosch, U. Steinhoff, J. Franke, L. Trahms, T. Schaeffter, F. Wiekhorst, Improved sensitivity and limit-of-detection using a receive-only coil in magnetic particle imaging, Phys. Med. Biol. (2018), https://doi.org/10.1088/1361-6560/aacb87.

[3] J. Wells, O. Kazakova, O. Posth, U. Steinhoff, S. Petronis, L. Bogart, P. Southern, Q.A. Pankhurst, C. Johansson, Standardisation of magnetic nanoparticles in liquid suspension, J. Phys. D. Appl. Phys. (2017), https://doi.org/10.1088/1361-6463/aa7fa5.

[4] S.D. L. Wöckel, J. Wells, O. Kosch, S. Lyer, C. Alexiou, C. Grüttner, F. Wiekhorst, Long-term stable measurement phantoms for magnetic particle imaginge, JMMM This Vol. (n.d.).

[5] J.F. Mendes, R.T. Paschoalin, V.B. Carmona, A.R. Sena Neto, A.C.P. Marques, J.M. Marconcini, L.H.C. Mattoso, E.S. Medeiros, J.E. Oliveira, Biodegradable polymer blends based on corn starch and thermoplastic chitosan processed by extrusion, Carbohydr. Polym. (2016), https://doi.org/10.1016/j.carbpol.2015.10.093.

[6] S. Biederer, T. Knopp, T.F. Sattel, K. Lüdtke-Buzug, B. Gleich, J. Weizenecker, J. Borgert, T.M. Buzug, Magnetization response spectroscopy of superparamagnetic nanoparticles for magnetic particle imaging, J. Phys. D. Appl. Phys. 42 (2009) 205007, , https://doi.org/10.1088/0022-3727/42/20/205007.

[7] S. Ziemian, N. Löwa, O. Kosch, D. Bajj, F. Wiekhorst, G. Schütz, Optimization of iron oxide tracer synthesis for magnetic particle imaging, Nanomaterials 8 (2018) 180, https://doi.org/10.3390/nano8040180.

[8] S.R. Snyder, U. Heinen, Characterization of magnetic nanoparticles for therapy and diagnostics, Bruker BioSpin Appl. Notes. 11 (2011) 1–4 http://www.bruker-biospin.com/mps-apps.html.

[9] J. Rahmer, J. Weizenecker, B. Gleich, J. Borgert, Signal encoding in magnetic particle imaging: properties of the system function, BMC Med. Imaging. 9 (2009) 4, https://doi.org/10.1186/1471-2342-9-4.

[10] J. Rahmer, J. Weizenecker, B. Gleich, J. Borgert, Analysis of a 3-D system function measured for magnetic particle imaging, IEEE Trans. Med. Imaging. 31 (2012) 1289–1299, https://doi.org/10.1109/TMI.2012.2188639.

[11] M. Graeser, T. Knopp, P. Szwargulski, T. Friedrich, A. Von Gladiss, M. Kaul, K.M. Krishnan, H. Ittrich, G. Adam, T.M. Buzug, Towards picogram detection of superparamagnetic iron-oxide particles using a gradiometric receive coil, Sci. Rep. 7 (2017), https://doi.org/10.1038/s41598-017-06992-5.

[12] A. Weber, F. Werner, J. Weizenecker, T.M. Buzug, T. Knopp, Artifact free reconstruction with the system matrix approach by overscanning the field-free-point trajectory in magnetic particle imaging, Phys. Med. Biol. 61 (2016) 475–487, https://doi.org/10.1088/0031-9155/61/2/475.